Available online at www.sciencedirect.com
ScienceDirect
Earth and Planetary Science Letters 248 (2006) 599–617
EPSL
www.elsevier.com/locate/epsl

Rock-magnetic and remanence properties of synthetic Fe-rich basalts: Implications for Mars crustal anomalies

Stefanie A. Brachfeld [a,*], Julia Hammer [b,1]

[a] Department of Earth and Environmental Studies, Montclair State University, Montclair, NJ 07043, USA
[b] Department of Geology and Geophysics, University of Hawaii, 1680 East-West Rd., Honolulu, HI 96822, USA

Received 25 January 2006; received in revised form 7 April 2006; accepted 7 April 2006
Available online 27 June 2006
Editor: S. King

Abstract

We characterized the magnetic mineral assemblage and remanence properties of a set of synthetic samples patterned on the meteorite-derived basalt composition A*, which contains 18.9% total FeO. Basalts were synthesized at conditions that track 4 oxygen fugacity (fO_2) buffer curves, from 3.4 log units below the quartz–fayalite–magnetite (QFM) buffer to 5 log units above QFM, and 6 cooling rates from 10^5 to 3 °C/h. The resulting array of samples was characterized using magnetic hysteresis loops, temperature dependence of saturation magnetization and saturation remanence (10 to 1000 K), and the acquisition and demagnetization of anhysteretic remanent magnetization (ARM) and thermoremanent magnetization (TRM). The magnetic mineral assemblage characteristics are strongly dependent on fO_2. Samples synthesized at the iron–wüstite (IW) buffer have a very low concentration of remanence-carrying grains, which are likely near the superparamagnetic-stable-single-domain boundary. Samples synthesized at the QFM and nickel–nickel oxide (NNO) buffers contain a slightly higher concentration of remanence-carrying grains, which are stable-single-domain to fine pseudo-single-domain particles, respectively. Samples synthesized at the manganese oxide (MNO) buffer contain the highest concentration of magnetic grains, which are up to 100 μm in diameter. The dominant Fe–Ti oxide produced is an Mg- and Al-bearing titanomagnetite with 2.4–2.7 Fe cations per formula unit. The Curie temperatures of the QFM samples are consistent with their electron-microprobe derived compositions. Those of the NNO sample set are very slightly elevated with respect to their electron microprobe derived compositions. The Curie temperatures of the MNO samples are elevated up to 200 °C above what they should be for their composition. We attribute the Curie temperature elevation to high-temperature nonstoichiometry of the titanomagnetite. The IW sample set acquired very weak TRMs with intensities of 0.02 to 0.5 A/m. This intensity of remanence is a factor of 50–500 too low to generate the observed 1000 nT anomalies detected on Mars by the Mars Global Surveyor MAG–ER experiment. The QFM, NNO, and MNO samples acquired TRMs up to 40 A/m in a 10-μT applied field, and up to 200 A/m in a 50-μT field, with little or no dependence on cooling rate. Our results suggest that Fe-rich melts that crystallize extensive titanomagnetite can generate an intensely magnetized layer in the Martian crust, even if the remanence was acquired in a weak field. The QFM sample set can easily account for the observed 1000-nT Mars magnetic anomalies, even in a magnetized layer as thin as 15–30 km.

Keywords: rock magnetism; planetary magnetism; TRM; titanomagnetite; Mars; magnetic anomalies; Mars Global Surveyor

* Corresponding author. Tel.: +1 973 655 5129; fax: +1 973 655 4072.
E-mail addresses: brachfelds@mail.montclair.edu (S.A. Brachfeld), jhammer@soest.hawaii.edu (J. Hammer).
[1] Tel.: +1 808 956 5996; fax: +1 808 956 5512.

0012-821X/$ - see front matter © 2006 Elsevier B.V. All rights reserved.
doi:10.1016/j.epsl.2006.04.015

1. Introduction

One of the many extraordinary results of the Mars Global Surveyor [MGS] mission was the detection of regions of intensely magnetized crust by the MAG/ER experiment [1–5]. This was unexpected, as Mars currently does not possess a global dynamo-generated field. The most intensely magnetized regions are located in the southern cratered highlands, the ancient [~4 Ga] densely cratered region south of the planetary dichotomy [1–5]. The anomalies are east–west oriented features that are 1000–2000 km long, up to 200 km wide, and alternate between positively and negatively magnetized bands [1–5]. These features dwarf terrestrial "sea-floor stripes," which range in width from 10 km generated by the slow-spreading Atlantic Ocean to 100 km generated by the fast-spreading East Pacific Rise.

Multiple mechanisms have been proposed to explain the alternating bands of positive and negative remanence. One possibility is past seafloor spreading on Mars in the presence of a reversing dynamo field [3]. The rate of seafloor spreading would have to be much faster than on Earth, or the frequency of field reversals much less than on Earth in order to account for the width of the magnetized regions. Conversely, the features may have been generated in a convergent boundary setting, in which differentially magnetized terranes were successively accreted [6]. Other plausible mechanisms include a succession of dike intrusions, in which the magma source has migrated north–south [7], or localized acquisition of a chemical remanent magnetization (CRM) due to hydrothermal alteration of the crust and associated formation of authigenic magnetite [8].

Equally or more intriguing than the spatial characteristics of the Mars anomalies are their intensity of remanence. The absence of a global field makes the Mars crustal anomalies easier to measure and map than their terrestrial counterparts. On Earth, any total field measurement is the sum of 3 components, the local field at the measurement location (H_E), the component of magnetization that the local field induces in the local rocks ($M_i = kH_E$), where k is the magnetic susceptibility of the rocks, and the remanent magnetization (M_R) carried by the rocks. The intensity of M_R is typically many orders of magnitude less than H_E and M_i, which makes isolating M_R a challenging process that depends on the availability and quality of H_E and k data for the region of interest. Since Mars does not possess an ambient field there is no induced component of magnetization, and the total field measurements made by MGS can be attributed entirely to M_R. The radial (vertical) component of magnetization approaches ± 1000 nT at the satellite altitude of 100 km [1–5]. In contrast, the strongest terrestrial anomaly has a projected intensity of 10 nT at satellite altitudes [4].

Several variables contribute to the observed intensity of the Mars crustal anomalies, including the mechanism of remanence acquisition, the intensity of the magnetizing field, the efficiency of the magnetic recording assemblage, the thickness and geometry of the magnetized layer, and any subsequent alteration of the remanent magnetization. Possible mechanisms of remanence acquisition include a thermoremanent magnetization (TRM), acquired when magma solidifies and cools through the Curie temperature of its constituent magnetic minerals in the presence of a magnetic field, or a CRM acquired when minerals crystallize below their blocking temperatures in the presence of a magnetic field. A primary TRM is the simplest assumption for the Mars crustal anomalies, given that the southern cratered highlands region is composed of basalt, as identified by the MGS Thermal Emission Spectrometer [9]. However, the magnetization was almost certainly modified, for example via large impacts that formed the Hellas and Argyre basins, both of which were likely demagnetized by the heat and shock pressure generated by the impact, and subsequent cooling on a field-free Mars after the dynamo shut off [10–14].

Constraints on both the Martian magnetic mineralogy and the intensity of the ancient Martian magnetic field have been derived from Martian Shergotty–Nakhla–Chassigny meteorites (SNCs). Titanomagnetite, the iron sulfide pyrrhotite, and chromite have all been observed as remanence carriers in SNC meteorites [15–23]. Hematite and titanohematite are very efficient recorders of TRM and CRM and could account for the intensity of the observed anomalies [24–29]. However, these minerals have not been observed in SNC meteorites, and the existing data regarding the oxygen fugacity of the Martian mantle and crust suggest that conditions are not oxidizing enough to form igneous hematite [30,31].

Attempts to constrain the intensity of the Martian magnetic field have used both heating and non-heating experiments on SNC meteorites, yielding estimates of 0.5 to 5 μT [18,19], or perhaps an order of magnitude stronger, comparable to the present-day terrestrial field [21]. However, the SNC meteorites are thought to be much younger than the southern cratered highlands [32]. It is therefore possible that neither the field intensity nor the magnetic mineralogy of the SNCs is applicable to the Mars crustal anomalies.

This study investigates the Mars crustal anomalies using a combined experimental petrology and rock

Table 1
Rock-magnetic parameters for the array of 24 synthetic basalts

Sample ID	fO_2 (ΔQFM)	Cooling rate (°C/h)	Composition	χ_{LF} (m^3/kg)	M_S (Am^2/kg)	M_R (Am^2/kg)	H_C (mT)	H_{CR} (mT)	M_R/M_S	H_{CR}/H_C	χ_{HF} (m^3/kg)	T_C (°C)	T_L (K)
IW buffer													
MA18	−3.44	10^5	–	1.87e−07	0.28	–	4.0	–	–	–	–	–	–
MA43	−3.44	231	–	3.50e−07	0.27	–	–	–	–	–	–	–	–
MA31	−3.44	72	–	1.92e−07	–	–	–	–	–	–	–	–	–
MA38	−3.44	19	–	5.41e−07	–	–	–	–	–	–	–	–	–
MA23	−3.44	6	–	5.85e−07	–	–	–	–	–	–	–	–	–
MA47	−3.44	3	–	5.26e−07	0.04	0.02	56.1	–	0.38	–	–	–	–
QFM buffer													
MA19	0.00	10^5		2.65e−07	–	–	–	–	–	–	–	–	–
MA44	0.00	231		6.50e−06	1.02	0.53	27.0	34.3	0.52	1.23	6.07e−07	285	57.5
MA32	0.00	72		3.76e−06	1.52	0.68	22.9	29.9	0.45	1.31	6.61e−07	385	55
MA39	0.00	19		1.84e−05	1.31	0.42	10.0	13.9	0.32	1.39	5.84e−07	315	62.5
MA24[a]	MH	6	$Fe_{2.25}Ti_{0.02}Al_{0.16}Mg_{0.57}O_4$[b]	9.95e−05	5.44	0.66	5.6	12.7	0.12	2.28	6.79e−07	485	50
MA48[a]	MH	3	$Fe_{2.01}Ti_{0.03}Al_{0.20}Mg_{0.7}O_4$[b]	9.40e−05	6.35	0.26	2.7	12.8	0.04	4.79	3.14e−07	510	40
NNO buffer													
MA20	0.82	10^5		3.52e−07	–	–	–	–	–	–	–	–	–
MA45	0.82	231		1.38e−05	1.77	0.58	17.7	25.4	0.33	1.44	6.25e−07	315	–
MA33	0.82	72	$Fe_{2.46}Ti_{0.30}Al_{0.19}Mg_{0.04}$	2.76e−05	2.20	0.34	8.4	16.7	0.16	1.99	7.21e−07	365	60
MA40	0.82	19		1.35e−05	1.06	0.31	11.3	15.9	0.30	1.41	3.52e−07	470	52.5
MA25	0.82	6	$Fe_{2.45}Ti_{0.33}Al_{0.17}Mg_{0.05}O_4$	3.61e−05	3.19	0.59	6.0	10.2	0.18	1.70	9.31e−07	350	60
MA49	0.82	3	$Fe_{2.53}Ti_{0.31}Al_{0.12}Mg_{0.03}O_4$	4.37e−05	3.07	0.51	6.9	16.0	0.17	2.33	9.34e−07	355	65
MNO buffer													
MA21	5.10	10^5	$Fe_{2.53}Ti_{0.05}Al_{0.12}Mg_{0.3}O_4$	5.83e−06	0.63	0.00	0.0	10.3	0.005	–	3.54e−07	491	25
MA46	5.10	231	$Fe_{2.57}Ti_{0.06}Al_{0.11}Mg_{0.26}O_4$	7.36e−05	8.33	0.94	8.8	26.5	0.11	3	7.11e−07	495	45
MA34	5.10	72	$Fe_{2.67}Ti_{0.08}Al_{0.11}Mg_{0.15}O_4$	9.78e−05	8.77	0.68	5.3	15.3	0.077	2.89	6.31e−07	490	45
MA41	5.10	19	$Fe_{2.41}Ti_{0.05}Al_{0.13}Mg_{0.41}O_4$	0.000109	10.90	0.39	2.5	10.1	0.036	4.07	3.83e−07	485	30
MA26	5.10	6	$Fe_{2.55}Ti_{0.12}Al_{0.15}Mg_{0.19}O_4$	9.85e−05	7.71	0.43	3.6	15.5	0.056	4.32	5.25e−07	475	45
MA50	5.10	3	$Fe_{2.48}Ti_{0.12}Al_{0.14}Mg_{0.26}O_4$	0.000105	12.60	0.43	2.1	9.7	0.034	4.63	5.55e−07	490	45

[a] Samples oxidized to magnetite–hematite buffer.
[b] Spinel phase.

magnetism approach. Iron-rich basalts were synthesized at conditions that track 4 different oxygen fugacity (fO_2) buffer curves, from 3.4 log units below the quartz–fayalite–magnetite buffer (QFM) to 5 log units above QFM, and 6 cooling rates from 10^5 to 3 °C/h [33,34]. At each set of experimental conditions we evaluate the mode, texture, and compositions of olivine, clinopyroxene, and iron–titanium oxides (presented in Hammer [34]), and bulk rock-magnetic properties and remanence characteristics (this paper). At each set of experimental conditions we examine the concentration of magnetic material, magnetic mineralogy, and remanence acquisition efficiency. We evaluate the controls of fO_2 and cooling rate on the magnetic mineral assemblage produced, and evaluate the potential of these samples to carry a TRM of sufficient intensity to generate 1000-nT field anomalies on Mars.

2. Methods

2.1. Samples

Our sample set consists of synthetic iron-rich basalts, synthesized under varying oxygen fugacity buffers and cooling rates. The experimental procedures are described in detail in Hammer [34]. Briefly, iron-rich, aluminum-poor basalt patterned on the composition of a basalt derived from the SNC meteorites (18.9% FeO) was synthesized from powdered oxide, carbonate, and phosphate reagents [34]. The mixture was heated to 1210 °C under four different fO_2 buffering conditions, controlled by means of solid phase assemblages: Fe–FeO (IW), SiO_2–Fe_2SiO_4–Fe_3O_4, (QFM), Ni–NiO (NNO), and MnO–Mn_3O_4 (MNO). Charges were cooled to below 200 °C at 6 cooling rates: ~10^5 °C/

h (quenched), 231, 72, 19, 6, and 3 °C/h. The experimental conditions produced an array of 24 samples, with 4 samples at each cooling rate and 6 samples at each fO_2 (Table 1). We note that two of the QFM runs did not remain at the buffering conditions, and oxidized to at least the Fe_3O_4–Fe_2O_3 (MH) buffer. These two samples are indicated in our data plots as MH. The amount of material generated in each run was typically several milligrams to a few tens of milligrams. The small sample sizes and irregular shapes necessitated the use of mass-normalized magnetic units. Splits of each sample were used for electron microscopy and characterization of magnetic properties.

2.2. Electron microscopy

Iron–titanium oxides were analyzed for grain size, texture, and composition using a JEOL J5900 Scanning Electron Microscope and a Cameca SX-50 Electron Microprobe (EMP) at the University of Hawaii-Manoa. EMP results for Fe–Ti oxides, olivine, pyroxene, and basaltic glass are described in detail in Hammer [34]. The Fe–Ti oxides were identified as either spinel-series titanomagnetite (Timt) or rhombohedral-series titanohematite. Titanomagnetite is inferred when the calculated mineral formula, assuming 4 oxygens, yields oxide totals near 100% and a cation total of 3. Titanohematite is inferred when the calculated mineral formula, assuming 3 oxygens, yields oxide totals near 100% and a cation total of 2 [34]. Maghemite is identified as yielding oxide totals of ~100% on 4-oxygen basis, but with stoichiometries that fall outside the ülvospinel–magnetite binary system [34].

2.3. Rock-magnetic characterizations

Rock-magnetic measurements were made at the Institute for Rock Magnetism (IRM), University of Minnesota. Magnetic susceptibility was measured using an AGICO KLY-2 Kappabridge. Magnetic hysteresis curves were measured from 10 to 300 K using a Princeton Measurements Corp. micro Vibrating Sample Magnetometer (μVSM 3900-04C) in room temperature configuration and using a liquid helium cryostat. Curie temperatures were determined from saturation magnetization versus temperature curves (M_S–T), measured from 20 to 700 °C in a 1-T field on the μVSM 3900-04 equipped with a furnace and flowing helium gas atmosphere. Magnetization was monitored during heating from 20 to 700 °C (heating curve) and during cooling from 700 °C back to room temperature (cooling curve). Magnetic hysteresis loops were measured before and after the M_S–T experiment in order to monitor thermochemical alteration of the sample.

Low-temperature order/disorder transitions were observed using a Quantum Design Magnetic Properties Measurements System (MPMS) via the temperature dependence of saturation isothermal remanent magnetization (M_R–T) imparted at 10 K and at 300 K, and via the temperature and frequency dependence of magnetic susceptibility $\chi(fT)$.

2.4. Remanence experiments

Anhysteretic remanent magnetization (ARM) and thermoremanent magnetization (TRM) were imparted to 23 and 19 of the 24 samples, respectively. ARM was imparted using a D-Tech Alternating Field Demagnetizer with ARM/pARM attachment. ARM samples consisted of a single large chip, or several small chips immobilized in Fiberfrax™ quartz cotton, packed inside a gelatin capsule. All specimens were AF-demagnetized in 3 mutually perpendicular directions at 200 mT prior to imparting ARM. ARM was imparted using a 100-mT peak alternating field and DC bias fields of 10, 20, 50, 100, and 200 μT. The intensity of ARM acquired at each field level was measured on a 2G model 760 single specimen cryogenic magnetometer at the Institute for Rock Magnetism. Following ARM acquisition, we stepwise AF-demagnetized the samples up to 100 mT.

TRM specimens consisted of a single large chip, or several small chips mixed in high-temperature cement and fixed to Princeton Measurements Corp. μVSM ceramic sample mounts. This aided in maintaining sample orientation within the TRM furnace and during measurements on the 2G cryogenic magnetometer. TRM was the last experiment performed on the samples, and was performed on the same chips used for hysteresis and low temperature experiments. All specimens were AF-demagnetized in 3 mutually perpendicular directions in a 200-mT peak alternating field prior to the TRM acquisition experiments.

TRM was imparted in a flowing argon gas atmosphere at field strengths of 10, 20, 50, and 100 μT. Samples were placed inside a quartz tube, which was connected to an argon gas cylinder. The quartz tube was placed inside a solenoid capable of generating steady applied fields from 10 to 100 μT. The field intensity and stability was monitored with a fluxgate magnetometer. The entire assembly was placed inside a set of 5 nested mu-metal shields in order to block out the ambient laboratory field. Curie temperatures determined via M_S–T experiments were used to select the temperature at which TRM was

imparted. All Curie temperature determinations were below 510 °C. Therefore, TRM was imparted at 550 °C as a function of applied field intensity. Samples were heated to temperature in the presence of the applied field, held at 550 °C, and then cooled in the presence of the applied field. The intensity of TRM acquired was measured using a 2G model 760 cryogenic magnetometer. Magnetic susceptibility was measured after each heating step on an AGICO KLY-2 Kappabridge to monitor thermochemical alteration of the specimen. Replicates of several samples were measured to assess sample homogeneity and TRM reproducibility.

3. Results

3.1. Electron microscopy

The iron–titanium oxides (Fe–Ti oxides) in the sample set display a wide variety of crystal sizes and textures (Fig. 1; see also Hammer [34]). Quenched samples and IW samples are glassy. Fe–Ti oxide grains are not clearly visible in any of these samples. Fe–Ti oxides increase in abundance with increasing fO_2 [34]. Samples synthesized at slower cooling rates have less glass and larger Fe–Ti oxide crystals. The Fe–Ti oxide crystals progress from skeletal, cruciform grains at fast cooling rates to euhedral grains that are up to 100 μm in size at slow cooling rates [34]. Long chains of Fe–Ti grains observed in the faster-cooled samples (>19 °C/h) are likely to be single crystals connected outside the plane of the thin section.

The dominant Fe–Ti oxide mineral is titanomagnetite ($Fe_{3-x}Ti_xO_4$, denoted Timt) with 2.4–2.7 Fe per formula unit (Table 1). A rhombohedral ilmenite-rich phase was not detected in any of the run products [34]. The abundance of Timt and the impurity content varies roughly systematically with fO_2. Fe–Ti oxide grains in the IW and QFM sample sets were smaller than the electron microprobe spot size and interaction volume. It is likely that compositional analyses on these small grains also included the surrounding crystals and glass. Therefore, compositions for these samples are not reported in Table 1. For grains larger than 10 μm we analyzed 10–20 spots per grain, and averaged the data to calculate the composition reported in Table 1. There is a significant amount of Mg and Al in the Timt, up to 0.6 cations per formula unit. Ti and Mg are inversely correlated. The NNO sample set is relatively Ti-rich and Mg-poor, whereas the MNO sample set is Mg-rich and Ti-poor. Only 3 of the 24 samples, MA24, MA41 and MA48, display 2-phase intergrowths (Fig. 1), two of

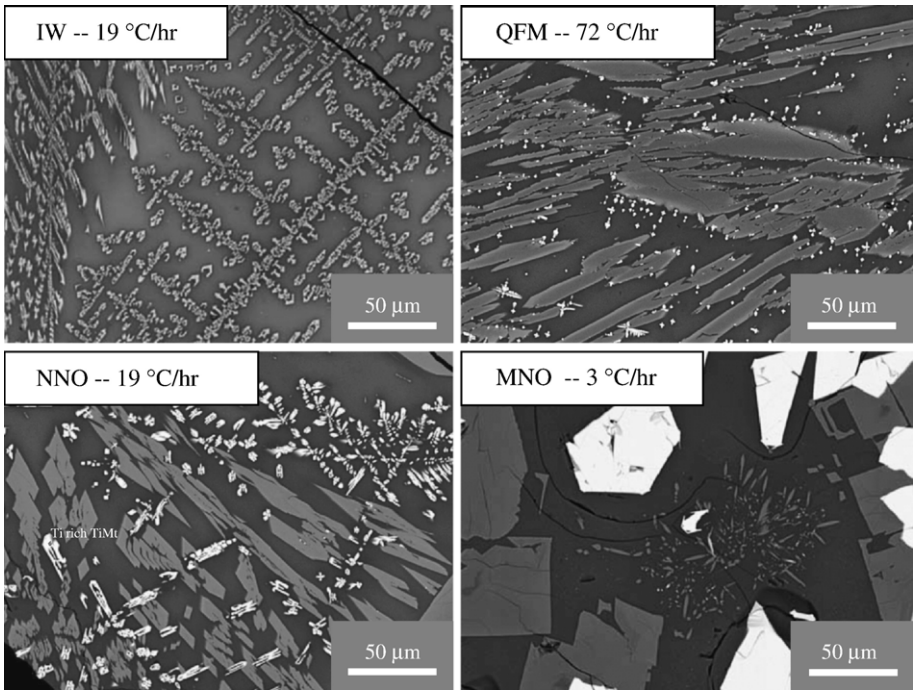

Fig. 1. Backscatter electron (BSE) images of selected samples. Iron oxide grain size and morphology is highly dependent on fO_2. See Hammer [34] for additional images.

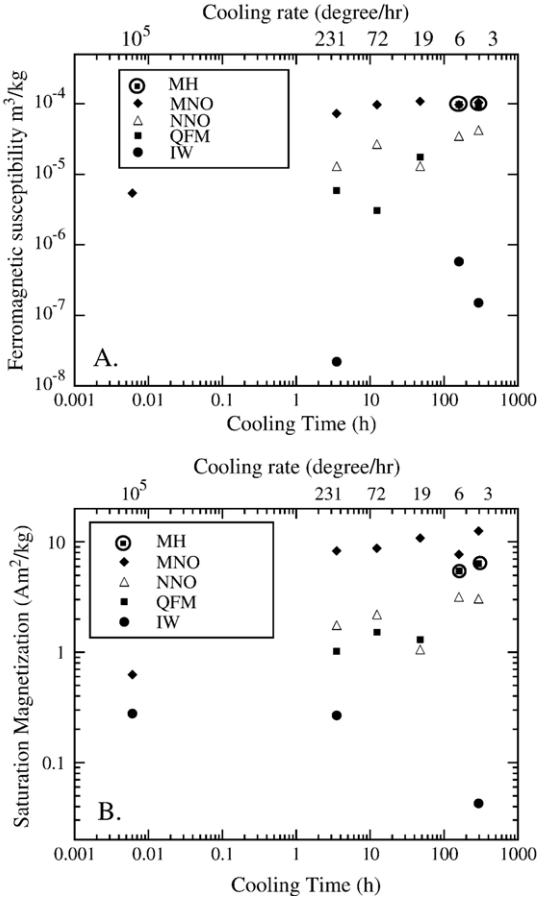

Fig. 2. (A) Ferromagnetic susceptibility (χ_F) and (B) saturation magnetization (M_S) of the sample array as a function of fO_2 and cooling rate.

which are the slow-cooled "QFM" samples oxidized to at least the MH buffer (MA24 and MA48). These samples contain titanohematite ($Fe_{2-y}Ti_yO_3$) with $y<0.08$ [34] (Figs. 4 and 5) as lamellae within maghemite. The host spinels have low Ti content ($x<0.03$) but high Mg and Al content, and their compositions plot to the right of the magnetite–ülvospinel solid solution line on the FeO–Fe_2O_3–TiO_2 ternary diagram (see [34] Figs. 4 and 5). The crystallographic orientations of the intergrown phases were determined using electron backscatter diffraction (EBSD). In sample MA41, the {0001} plane poles of the rhombohedral phase (titanohematite) are coincident with the {111} plane poles of the host spinel phase (maghemite). This crystallographic relationship of intergrown Fe–Ti oxides is diagnostic of high-temperature oxidation and oxyexsolution of titanomagnetite, and the observed cation deficiency of the host is characteristic of low-temperature oxidation to maghemite [35,36].

3.2. Room-temperature rock-magnetic characterizations

The concentration of magnetic material in the synthetic basalts was monitored using low-field magnetic susceptibility (χ), high-field magnetic susceptibility (χ_{HF}) and saturation magnetization (M_S) corrected for paramagnetic (i.e., high-field) contributions. The quenched sample set and the IW sample set have weak values of bulk magnetic susceptibility, on the order of $1–5*10^{-7}$ m^3/kg, most of which is carried by paramagnetic minerals and glass (Table 1 and Fig. 2). Several of the quenched sample set and the IW sample set show no hysteresis and a linear M–H curve, hence there is no difference between low-field and high-field susceptibility, and no high-field corrected M_S reported for these samples. Cooling rate has little control on χ and M_S. χ and M_S increase with higher fO_2 values, i.e., more oxidizing conditions generate a higher concentration of magnetic material. We estimated the vol.% of titanomagnetite in the sample set using the paramagnetic-corrected M_S values (Table 1), which were converted to volume-normalized units (A/m) using 2900 kg/m^3 as the density of basalt [37], and 48 Am^2/kg as the saturation magnetization for titanomagnetite with 2.5 Fe per formula unit [38]. This calculation yields <1% magnetite for the IW samples, 1–2% for the QFM samples, 1–4% for the NNO samples, and 9–20% for the MNO and MH samples. These magnetically derived concentration estimates closely match the quantitative vol.% magnetite contents derived via image processing, [34].

Magnetic hysteresis parameters are displayed in Fig. 3. 2 of the 4 quenched samples and 3 of the 6 IW samples display purely paramagnetic magnetization versus applied field (M–H) curves. The QFM, NNO, and MNO hysteresis

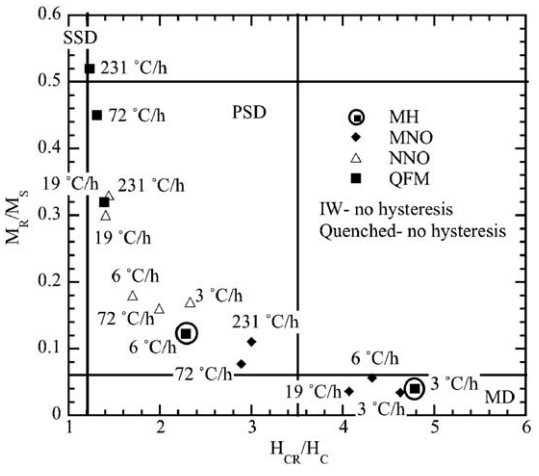

Fig. 3. Magnetic hysteresis parameters for the QFM, NNO, and MNO sample sets displayed on a Day Plot [39].

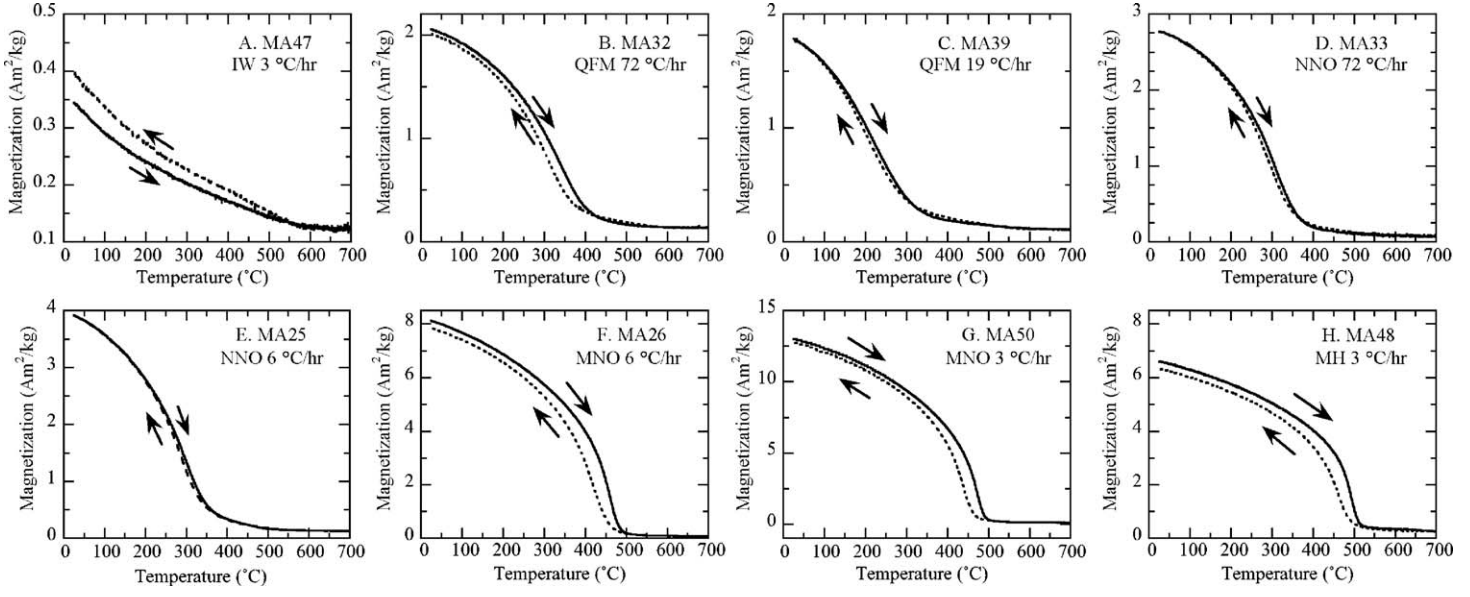

Fig. 4. M_S–T curves for selected samples measured in a 1-T applied field from 20 to 700 °C. Solid lines denote heating curves. Dashed lines denote cooling curves. The samples have well-defined Curie temperatures between 285 and 510 °C. All samples have nearly perfectly reversible heating and cooling curves, suggesting little or no thermochemical alteration during the measurement.

parameters fall within the stable-single-domain (SSD), pseudo-single-domain (PSD) and multidomain (MD) fields on a "Day Plot" [36,39]. Oxygen fugacity has a strong control on hysteresis parameters. The QFM, NNO and MNO sample sets form distinct clusters with minimal overlap. The more reduced samples plot towards the upper left of the Day Plot, and the samples move towards the lower right with increasing fO_2. Within each fO_2 group, samples move from upper left to lower right with increasing cooling time. The oxidized QFM samples plot with the MNO group. Both of these samples contain 2 phase intergrowths of variably maghemitized spinel and titanohematite, and both plot within the MD region of a Day Plot. Apparently, the subdivision of grains by lamellar intergrowths during high-temperature oxyexsolution did not decrease the magnetic domain size of these Fe–Ti oxides.

3.3. Temperature-dependent order–disorder transitions

High-temperature M_S–T curves were measured in order to determine each sample's Curie temperature, to select the appropriate temperature for TRM acquisition, and to assess the samples' susceptibility to thermochemical alteration during heating. The entire IW sample set and all but one quenched sample yielded paramagnetic M_S–T curves, with no clear order/disorder transitions evident during heating or cooling (Fig. 4A). The one exception is the MNO quenched sample (MA21), which yielded a well-defined Curie temperature at 491 °C. All remaining samples yielded reversible heating and cooling curves and well-defined Curie temperatures between 285 and 510 °C (Table 1 and Fig. 4).

None of the samples yielded Curie temperatures consistent with pure magnetite or pure hematite. The Curie temperatures of the MNO sample set and the two oxidized QFM samples range from 475 to 510 °C. The NNO and QFM samples have Curie temperatures between 285 and 385 °C, with the exception of sample MA40. Within each fO_2 group, cooling rate has no influence on Curie temperature.

Low temperature M_R–T curves indicate the presence of a remanence-carrying phase in the quenched and IW samples. None of the samples display the magnetite Verwey transition, nor is there a suggestion of the Verwey transition in the first derivative of the M_R–T data (Fig. 5). The fast-cooled IW samples (>19 °C/h) display rapid unblocking below 20 K, consistent with either superparamagnetic (SP) behavior or thermal unblocking of a paramagnetic phase that is ordered at very low temperatures, possibly Fe-rich regions of the basaltic glass. These samples lose >90% of the remanence imparted at 10 K during warming to 300 K. The slow-cooled IW samples show a more

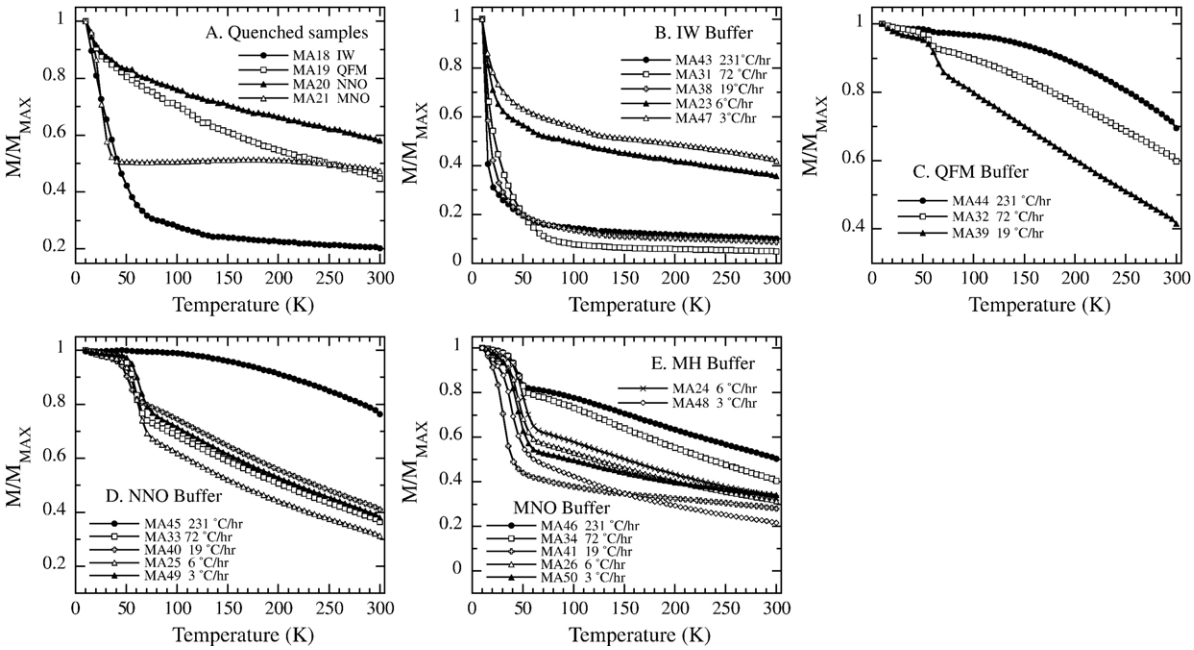

Fig. 5. Low temperature M_R–T curves for selected samples. M_R was imparted in a 2.5-T field at 10 K. The samples display abrupt, large drops in remanence at temperatures of 20–65 K. This is too low to be the magnetite Verwey transition. The observed order/disorder transitions may be titanomagnetite isotropic points or unpinning of domain walls due to decreasing magnetocrystalline anisotropy.

gradual loss of remanence during warming, and retain 30–40% of the initial remanence upon reaching 300 K.

Frequency and temperature dependence of magnetic susceptibility was measured to further investigate if superparamagnetic particles are present. The fast-cooled IW samples show purely paramagnetic curves with no frequency dependence of susceptibility (Fig. 6A). The entire MNO sample set, including the quenched sample (MA21), shows strong frequency dependence below 100 K (Fig. 6B, C, D). Frequency dependence of magnetic susceptibility below 100 K is a characteristic of titanomagnetite (M. Jackson and B. Moskowitz, unpublished data). The quenched MNO sample (MA21) also shows a decrease in the peak $\chi(T)$ value as function of frequency, and a shift in the temperature at which the peak χ occur (Fig. 6B). These behaviors can be caused by the presence of superparamagnetic particles [40]. However, coarse-grained synthetic titanomagnetites also exhibit a frequency-dependent shift in the temperature at which the peak χ occurs (M. Jackson and B. Moskowitz, unpublished data). None of the samples display frequency dependence of susceptibility above 100 K. While M_R–T and ARM results are consistent with, but not diagnostic of, the presence of ultrafine grains near the SP/SSD boundary, $\chi(fT)$ results were inconclusive.

The QFM, NNO, and MNO samples display abrupt drops in the intensity of remanence below 65 K (Table 1 and Fig. 5). For the MNO sample set the remanence drop occurs at 25–45 K. The samples show a progressive loss of M_R below the remanence drop. Above the remanence drop there is only a 10% decrease in the intensity of M_R. Similar behavior was reported for synthetic 2-mm single crystals of titanomagnetite and natural iron-rich titanomagnetites with 0.05 to 0.40 Ti cations per formula unit [41,42]. The Ti content of the MNO samples is 0.05–0.12 cations per formula unit, but the sum of Ti+Al+Mg is 0.34 to 0.59 cations per formula unit. These features are likely magnetic isotropic points (denoted T_I) where the first magnetocrystalline anisotropy constant K1 is briefly zero as it changes sign [36,41,42]. Remanence imparted below the isotropic point is partially demagnetized upon warming through T_I due to the shift in the easy axes of magnetization from the [100] direction below T_I to the [111] direction above T_I [36,41,42].

The remanence drop is suppressed or absent in the fast-cooled (231 °C/h) QFM and NNO samples (Fig. 5). For all other QFM and NNO samples the transition temperatures occur at 50–65 K. The shape of the M_R–T curves are similar to those reported for synthetic titanium-rich titanomagnetite (compositions TM55–

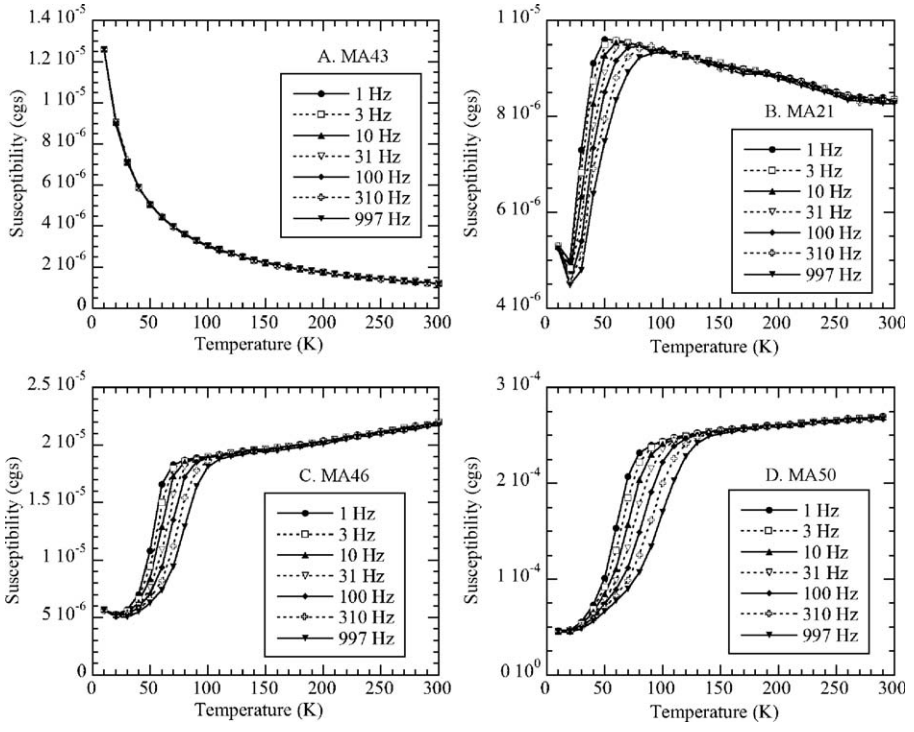

Fig. 6. Magnetic susceptibility as a function of applied field frequency and temperature. All samples have substantial frequency dependence below 100 K, a behavior observed in synthetic titanomagnetites (M. Jackson and B. Moskowitz, unpublished data).

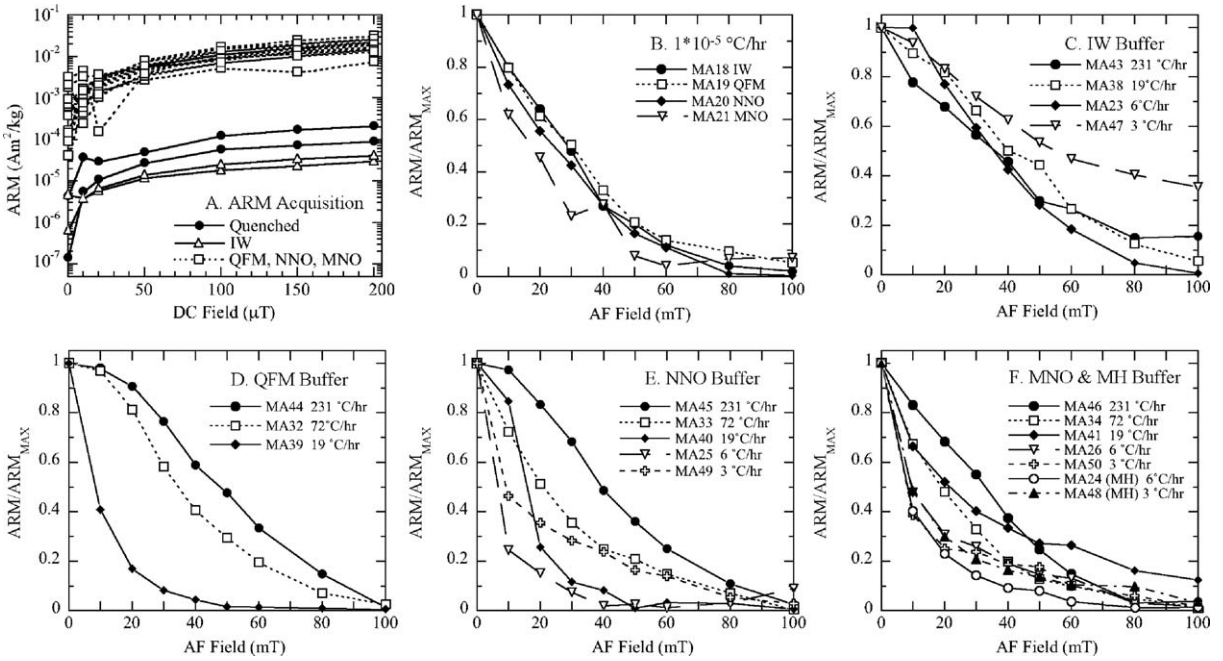

Fig. 7. (A) ARM acquisition as a function of DC bias field. Quenched and IW samples carry a measurable ARM. The intensity of ARM is several orders of magnitude stronger for the QFM, NNO, and MNO samples, but with no systematic dependence on fO_2 or cooling rate. (B–F) Alternating field (AF) demagnetization of ARM for the (B) quenched, (C) IW, (D) QFM, (E) NNO, and (F) MNO sample sets.

TM61) [41]. There is little or no loss of M_R below the transition temperature. Above the transition temperature the intensity of remanence continues to decay up to 300 K, with a 40% drop in the intensity of remanence. The NNO samples have a high Ti content, 0.31 to 0.33 cations per formula unit, but the sum of Ti+Al+Mg spans the same range of values as the MNO sample set. Moskowitz et al. [41] suggested that the remanence drops for the titanium-rich titanomagnetite (TM55–TM61) were not isotropic points, but instead related to the decrease in magnetocrystalline anisotropy and the associated widening and unpinning of domain walls, or possibly related to Jahn–Teller lattice distortions [41].

3.4. Remanence experiments

Although the quenched and IW sample sets display paramagnetic *M–H* curves, both sample sets acquired a measurable anhysteretic remanent magnetization (ARM) (Fig. 7). The quenched and IW samples' intensity of ARM was 2 orders of magnitude above the empty background of the 2G superconducting magnetometer. Therefore, the quenched and IW samples both contain a remanence-carrying phase, although its' concentration is too low to measure on the vibrating sample magnetometer and too small to image on the SEM. The quenched samples all have similar AF demagnetization curves (Fig. 7), with a median destructive field (MDF) of 18–30 mT. The IW samples acquired a slightly weaker ARM but were more resistant to AF demagnetization, with a MDF range of 35–57 mT (Fig. 7). The QFM, NNO, and MNO sample sets acquired an ARM that was 2–3 orders of magnitude stronger than the quenched and IW samples. There is no systematic relationship between fO_2 and the intensity of ARM acquired, nor is there a systematic relationship between cooling rate and the intensity of ARM acquired.

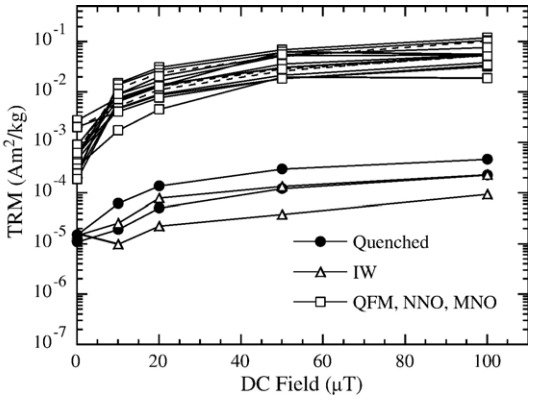

Fig. 8. TRM acquisition as a function of applied field strength, from 10 to 100 μT.

Table 2
Intensity of ARM and TRM acquired in weak (10 μT) and strong (50 μT) applied fields

Sample ID	Cooling rate (°C/h)	$ARM_{50\ \mu T}$ (mAm^2/kg)	$TRM_{10\ \mu T}$ (mAm^2/kg)	$TRM_{50\ \mu T}$ (mAm^2/kg)	$TRM_{10\ \mu T}$/SIRM	$TRM_{50\ \mu T}$/SIRM
IW buffer						
MA18	10^5	0.028	0.019	0.122	–	–
MA43	231	0.012	0.010	0.038	–	–
MA31	72	–	–	–	–	–
MA38	19	0.014	–	–	–	–
MA23	6	0.138	–	–	–	–
MA47	3	2.41	0.026	0.137	0.002	0.009
QFM buffer						
MA19	10^5	0.00	–	–	–	–
MA44	231	8.35	15.33	69.60	0.03	0.13
MA32	72	6.19	14.10	61.91	0.02	0.09
MA39	19	6.45	7.32	31.36	0.02	0.08
MA24[a]	6	3.54	11.84	50.40	0.02	0.08
MA48[a]	3	3.88	1.75	19.98	0.01	0.08
NNO buffer						
MA20	10^5	0.05	–	–	–	–
MA45	231	6.14	7.77	30.69	0.01	0.05
MA33	72	4.89	4.74	18.61	0.01	0.05
MA40	19	2.80	9.12	52.93	0.03	0.17
MA25	6	4.13	5.25	26.10	0.01	0.04
MA49	3	6.05	6.62	62.72	0.01	0.12
MNO buffer						
MA21	10^5	0.05	0.06	0.30	0.02	0.10
MA46	231	8.13	6.57	36.30	0.01	0.04
MA34	72	7.85	4.95	21.60	0.01	0.03
MA41	19	5.75	4.09	18.63	0.01	0.05
MA26	6	5.77	7.28	28.60	0.02	0.07
MA50	3	5.72	9.20	56.28	0.02	0.13

[a] Samples oxidized to magnetite–hematite buffer.

However, a systematic relationship is observed during AF demagnetization (Fig. 7). Slower cooled samples are magnetically "softer," with MDFs of 5–10 mT. Rapidly cooled samples are more resistant to AF demagnetization, and the MDF progressively increases for faster cooling rates.

Thermal remanent magnetization was imparted to the samples as a function of applied field strength (Fig. 8). TRM acquired is not linearly proportional to the applied field strength. Several samples acquired their maximum TRM at 50 μT, and the remaining samples experienced only a slight gain in TRM between the 50-μT and 100-μT steps. TRM intensity imparted at 10 μT is 0.01–0.06 mAm^2/kg for the IW samples, and 4–15 mAm^2/kg for the QFM, NNO, and MNO samples (Table 2). TRM intensity imparted at 50 μT is 0.05 to 0.5 mAm^2/kg for the IW samples, and 20–70 mAm^2/kg for the QFM, NNO, and MNO samples. The QFM samples and slowest cooled MNO samples have the highest intensity of TRM at each field step (Table 2). The TRM recording efficiency, calculated as TRM divided by saturation isothermal remanent magnetization (SIRM), ranges from 0.01 to 0.17 (Table 2).

4. Discussion

Our suite of rock-magnetic data and electron microscopy analyses allow a comprehensive characterization of the magnetic mineral assemblage in our sample set. Such comprehensive analysis is always desirable, but not always possible in SNC meteorite samples due to the scarcity of material and the destructive nature of heating experiments, the latter of which are required for Curie temperature determinations and TRM experiments. Here we evaluate the constraints that each rock-magnetic result can place on modeling the Mars magnetic source.

4.1. Magnetic recording assemblage

The rock-magnetic properties of our sample set are strongly dependent on fO_2. QFM samples contain SSD and fine PSD Timt grains. NNO and MNO samples contain coarser PSD and MD Timt grains. Within each fO_2 group there is a domain-state dependence on cooling rate. Although the majority of samples fall in the PSD region of a Day Plot [39], hysteresis parameters represent the average response of the entire sample to the applied field. Mixtures of grain sizes can produce bulk hysteresis parameters that appear PSD [36]. We suspect that the IW samples, which appear purely paramagnetic in hysteresis experiments, contain a low concentration of fine SP/SSD grains. Similarly, we suspect that the QFM and NNO samples, which mainly show >10-μm grains in the BSE images, also contain a population of fine SP/SSD titanomagnetite.

Several of the BSE images of the QFM and NNO samples show very small (<1 μm) bright grains that may be Timt, but confirmation of mineralogy by energy-dispersive x-ray spectrometry or electron probe microanalysis is not possible because they are smaller than the SEM and EMP interaction volume. For the quenched, IW, QFM and NNO sample sets, the presence of fine and ultrafine grains is suggested by the ARM demagnetization data. ARM preferentially activates PSD and SSD grains. Therefore, a population of fine grains that may be volumetrically low and overwhelmed by MD grains and paramagnetic minerals during in-field measurements of χ and M_S can be observed using ARM. Although the hysteresis parameters of the quenched and IW samples appear purely paramagnetic, these samples acquired a weak but measurable ARM. The AF demagnetization curves suggest SSD particles for the IW samples and the sample set cooled at 231 °C/h. These samples may contain fine magnetic particles within the basaltic glass or exsolved inside silicate minerals.

The magnetic phase in nearly all of the samples is Mg- and Al-bearing titanomagnetite. The average Timt composition for the NNO and MNO samples has 2.4–2.7 Fe cations, and 0.6 to 0.3 cations comprised of Ti, Mg, and Al (Table 1). While the amount of Mg and Al substitution appears high, our compositions are comparable to the Fe–Ti spinels and Fe–Ti–Cr spinels recently observed in SNC meteorites [23]. Titanium, aluminum, and magnesium ions are all diamagnetic. Al^{3+} and Mg^{2+}, like Ti^{4+}, decrease the saturation magnetization and Curie temperature as they substitute for Fe^{2+} and Fe^{3+}. Timt grains with 2.4 to 2.7 Fe cations per formula unit should have Curie temperatures in the range of 180 to 350 °C [38]. While the QFM and NNO samples have Curie temperatures consistent with, or only slightly elevated with respect to the microprobe-derived Fe/(Ti+Al+Mg) ratio, the 6 MNO and the 2 MH sample sets have Curie temperatures that are 100 to 200 °C higher than expected.

The disparity between the Curie temperatures expected on the basis of electron microprobe-determined Fe content and those measured via M_S–T may arise from high-temperature nonstoichiometry. The MNO sample set likely contains stable titanomagnetite grains that incorporated vacancies while rapidly crystallizing at magmatic temperatures. Our observations are similar to studies of synthetic TM60, which demonstrated that above 1000 °C titanomagnetite can accommodate limited deviations from stoichiometry within its stability field [43,44]. The degree of nonstoichiometry increases as a function of temperature and fO_2, and is accompanied by elevated Curie temperatures [43,44].

The MH samples, MA24 and MA48 (cooled at 6 °C/h and 3 °C/h, respectively) and one MNO sample (MA41 cooled at 19 °C/h) display sandwich-type lamellae of Ti-poor, Mg-rich titanohematite within a strongly nonstoichiometric spinel fitting the chemical definition of maghemite [35]. The lamellae presumably formed during high temperature oxyexsolution of the mildly cation-deficient primary phase. The drift of the spinel compositions in MA24, MA48, and MA41 away from the magnetite–ülvospinel solid solution line (see [34] Fig. 4) suggests that maghemitization of the host grains occurred during the lower-temperature portions of the cooling experiments.

Despite the presence of maghemite, the M_S–T curves for MA24, MA48, and MA41 are nearly perfectly reversible (Fig. 4). It is possible that the Curie curves are dominated by the Mg-rich titanohematite lamellae. However, the saturation magnetization of titanohematite is weaker than that of maghemite. While we have not quantified the vol.% of each phase, the maghemite appears to be more volumetrically significant in all 3 samples, and is expected to make a stronger contribution to M_S. If the maghemite dominates the Curie curves, then reversible behavior during heating and cooling cycles is contrary to the typical observations for maghemite and titanomaghemite. Maghemite inverts to hematite during heating in air or in a vacuum, and titanomaghemite inverts to a titanium-rich rhombohedral phase plus a titanium-poor spinel [36,45]. We speculate that the maghemite in these samples is stable with respect to hematite up to temperatures of 490–510 °C (Fig. 4h), possibly related to the large amount of Al and Mg substitution in the crystals (Table 1). Our observations are similar to those reported by Özdemir and Banerjee [46], who reported that synthetic maghemite crystals remained stable during

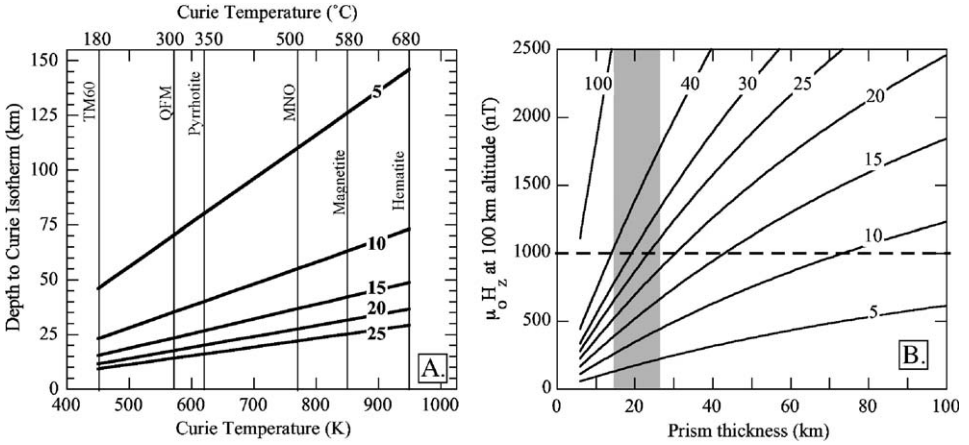

Fig. 9. (A) Depth to the Curie isotherm as a function of geothermal gradient, from 5 to 25 K/km (bold curves) and a surface temperature of 220 K. The average Curie temperatures of the QFM and MNO sample sets are shown, along with the Curie temperatures of TM60, pyrrhotite, magnetite, and hematite. If the geothermal gradient on Mars was high (25 K/km) at 4 Ga, the magnetized layer is constrained to be less than ~28-km thick (indicated by grey bar). (B) Intensity of the vertical magnetic field anomaly over a 200-km-wide prism of variable thickness as a function of volume magnetization (5 to 100 A/m). The generation of 1000-nT anomalies at a satellite altitude of 100 km in a layer constrained to be less than 28 km thick requires volume magnetizations of 25–40 A/m.

heating up to 500–510 °C, followed by incomplete inversion to hematite at 510–660 °C. The authors observed that 65% of the original maghemite remained unchanged following heating. Similarly, we suspect that the maghemite in MA24, MA41, and MA48 experienced incomplete inversion to hematite, hence the nearly reversible heating and cooling cycles.

The Curie temperature of the magnetic recording assemblage constrains the thickness of the magnetized layer on Mars. To investigate the required thickness of the Mars magnetized layer we calculated the depth to the Curie isotherm of our QFM and MNO sample sets, along with magnetite, hematite and pyrrhotite (Fig. 9A). We used a Mars surface temperature of 220 K (−55 °C) and linear geothermal gradients of 5–25 K/km. The use of linear gradients is too simplistic if there are heat-producing radiogenic elements in the Martian crust, which would result in shallower Curie isotherms than those calculated here [47]. However, this simple calculation can serve as an initial approximation of the required layer thickness.

For a low geothermal gradient of 5 K/km, the average Curie temperature of our QFM sample set is reached at ~75 km and the average MNO Curie temperature is reached at ~110 km. For a low geothermal gradient, the thickness of the magnetized layer can potentially be quite large. However, the geothermal gradient at 4 Ga when the magnetization was acquired was likely much higher [48]. For a geothermal gradient of 25 K/km, the Curie temperatures of the QFM and MNO sample sets are reached at 14 km and 23 km, respectively. The Curie temperatures of pure pyrrhotite, magnetite, and hematite are reached at 16, 25 and 28 km, respectively. For a high geothermal gradient, the magnetized layer is relatively thin for all of the possible recording minerals. In this case, a very high intensity of remanence is required to generate the observed 1000-nT anomalies at 100-km altitude.

The intensity of remanence required to generate a given vertical field anomaly H_Z was calculated by modeling a uniformly magnetized block as the region between two parallel sheets of magnetic poles, one at the base of a prism with magnetization $+M_Z$ and one at the top of a prism with magnetization $-M_Z$ [49]. We used a block that is 200-km wide in the X-direction, infinitely long in the Y-direction, and varying in thickness from 5 to 100 km (Fig. 9B). The contours in Fig. 9B show the resulting vertical field anomaly H_Z as a function of prism thickness and intensity of M_Z. For a block constrained to a thickness of less than ~30 km by the likely Curie isotherms, the required values of M_Z necessary to generate an anomaly of 1000 nT at a satellite altitude of 100-km range from 25 to 40 A/m. The required values of M_Z would be higher for blocks that are narrower in the X-direction. The M_Z values required to produce the observed intensity of remanence from a relatively thin layer far exceed the NRM values of most terrestrial basalts, which range from <1 to 15 A/m [50–57].

4.2. Intensity of TRM

A key question in this study is to assess whether iron-rich basalt acquires a TRM that has significantly higher

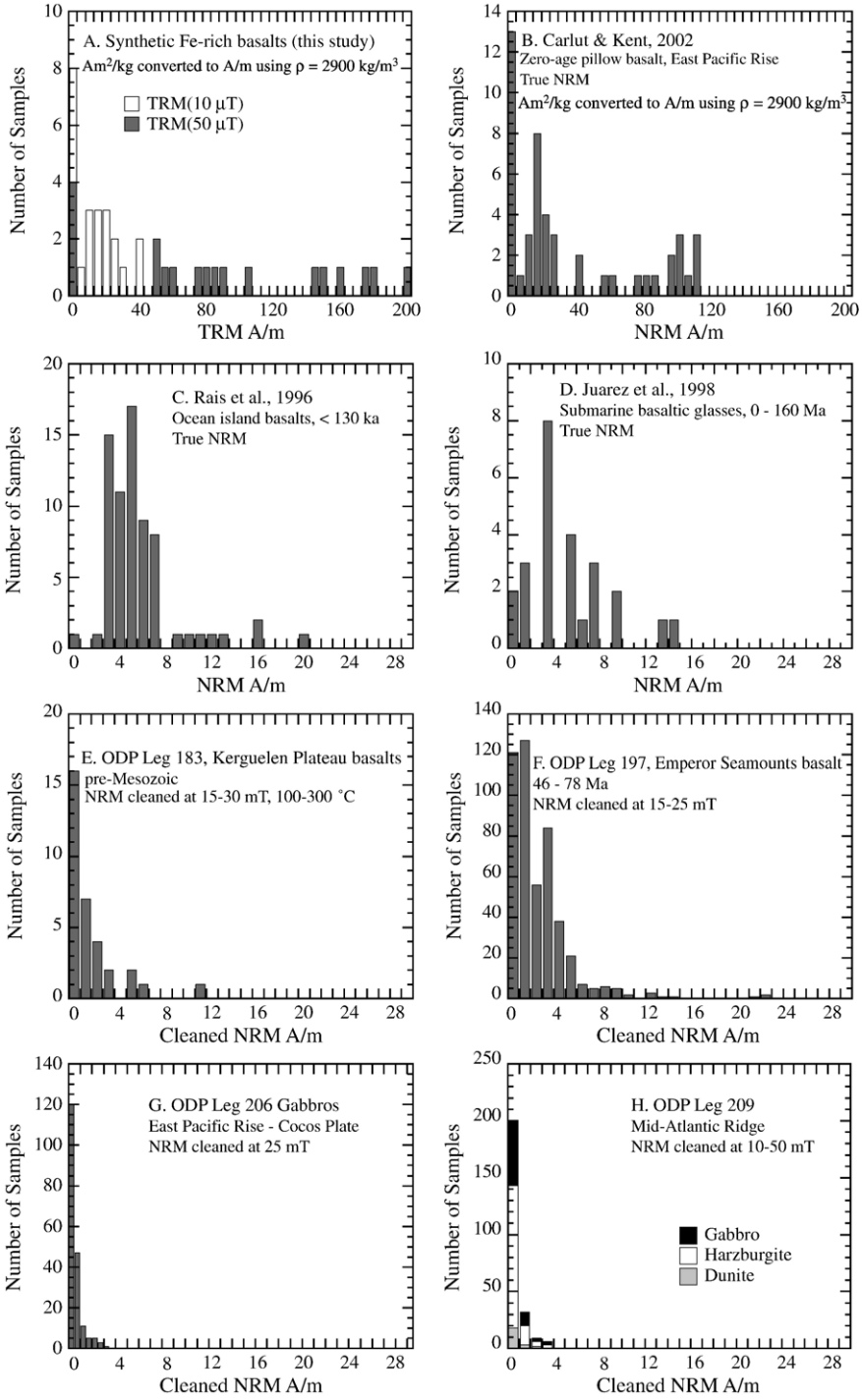

Fig. 10. TRM intensity of the synthetic Mars basalts acquired at 10 μT and 50 μT compared with cleaned NRM intensity of terrestrial basaltic glass, basalt, gabbro, and ultramafic crustal rocks. The NRMs of the Ocean Drilling Program samples have been AF demagnetized or thermally demagnetized to remove the drilling overprint [50–54]. True NRMs (no demagnetization) are shown for samples collected via 1 in. paleomagnetic drill cores [55] or via dredge hauls [56,57].

intensity than typical MORB. In order to compare the synthetic basalt intensities to terrestrial basalts, we have converted our mass-normalized TRMs (Am^2/kg) to volume-normalized TRMs (A/m) using 2900 kg/m^3 for the density of basalt [37]. The oxide-rich MNO samples are likely to have higher densities than the oxide-poor and silicate-rich IW samples. However, a density difference of ± 100 kg/m^3 causes only a ±3% change in the volume-normalized TRM value. Given that the TRM values for the MNO sample set are nearly 3 orders of magnitude higher than the IW sample set, we consider a few percentage points of uncertainty negligible for this calculation. Natural remanent magnetization (NRM) intensities of terrestrial basalt, basaltic glass, and gabbro were compiled from subaerial and submarine studies, the latter coming mainly from Ocean Drilling Program (ODP) expeditions. Several ODP legs have targeted oceanic crust at both fast and slow spreading centers, ocean island basalts, exposures of lower gabbroic crust and mantle peridotite, and large igneous provinces [50–54].

The intensity of NRM in both subaerial and submarine basalts can be misleadingly high. For example, basalts collected on La Réunion Island have NRM intensities of <1 to 20 A/m [55]. However, NRM intensities greater than ~15 A/m were attributed to lightning strikes, hence they are a saturation isothermal remanent magnetization (SIRM) acquired in a very strong field rather than a thermal remanent magnetization acquired in the ambient terrestrial field [55].

Several ODP legs have reported very high NRM intensities for oceanic crustal rocks, exceeding 20 A/m. However, these samples are affected by a secondary component of magnetization acquired during drilling. This "drilling overprint" has been repeatedly observed and described in both sediments and igneous rocks [50–54]. In order to estimate typical NRM intensity ranges for terrestrial rocks we have compiled "cleaned NRM" values (denoted NRM_{Cl}). Cleaning consists of step-wise AF demagnetization or thermal demagnetization and monitoring of the remanence vector to determine when the drilling overprint has been removed and the characteristic remanence (ChRM) has been isolated. The drilling overprint often accounts for >90% of the initial NRM [50–54]. One-inch paleomagnetic drill cores from subaerial sites (that are free of lightning-induced SIRM) and dredge hauls are free of the drilling overprint. Hence the true NRM is reported for dredge samples in Fig. 10 [55–57].

Our NRM_{Cl} compilation was constructed using the intensity of remanence at the lowest AF or thermal demagnetization step that defines the ChRM. For example, if the shipboard paleomagnetism team reported that the ChRM was determined from the 15–50 mT AF demagnetization levels, then the cleaned NRM reported here is the intensity of NRM at the 15-mT step. The character, coercivity, and intensity of the drilling overprint varies with rock type and magnetic mineral assemblage of each sample. Therefore, the cleaning method varies for the four ODP legs considered here, and includes AF demagnetization data from the 10–30 mT steps and thermal demagnetization data from the 100–300 °C steps. While cleaned NRM intensities are certainly lower than true NRM intensities, they nevertheless enable us to estimate the order of magnitude of NRM intensity for terrestrial rocks.

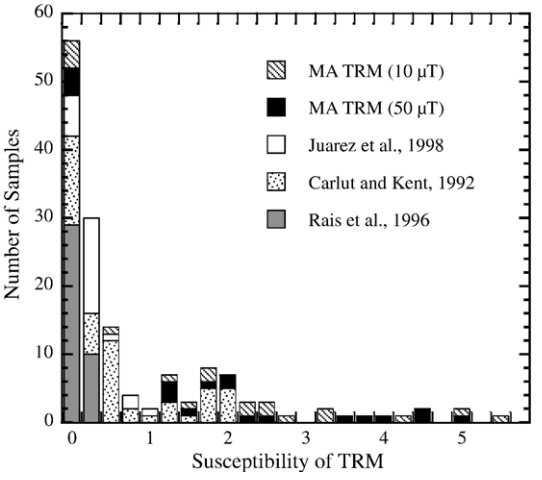

Fig. 11. Susceptibility of TRM and NRM (χ_{TRM} and χ_{NRM}, respectively) for selected data sets from Fig. 10. χ_{TRM} is calculated from NRM (or NRM_{CL}) intensity and the intensity of the magnetizing field determined from Thellier–Thellier absolute intensity analyses.

Our synthetic Fe-rich basalts have a very high intensity of TRM compared with the cleaned NRM of terrestrial samples, in which iron contents range from 4% to 15% (Fig. 10). The intensity of TRM acquired by our sample set varies as a strong function of fO_2. The IW sample set acquired a weak but measurable TRM on the order of 0.02–0.5 A/m. The QFM, NNO, and MNO sample sets acquired TRM with intensities of 10–40 A/m in a 10-μT field, and up to 100–200 A/m in a 50-μT field (Fig. 10). The intensity of TRM acquired by the QFM sample set in a 10-μT field has a higher intensity than most terrestrial basalts, basaltic glasses, and gabbros. TRM acquired by the QFM, NNO, and MNO samples in a 50-μT field is substantially higher than terrestrial samples (Table 2 and Fig. 10). Only the zero-age terrestrial pillow basalts from the East Pacific Rise match this intensity of remanence [56]. Carlut and Kent attributed their high NRM intensities to the young age of the samples, absence of

alteration, and possibly an enhanced magnetizing field due to a strong local magnetic anomaly.

Samples in the NRM_{Cl} compilation span a wide range of latitudes and a large range of ages. To remove the impact of geomagnetic field spatial and temporal variations on NRM intensity and degree of time-dependent alteration, we calculate and compare the susceptibility of TRM (Fig. 11). We define the susceptibility of TRM [χ_{TRM}] as TRM/H for the synthetic Mars basalts, where H is the applied field strength, or NRM_{Cl}/H_A for terrestrial samples, where H_A is the ancient magnetizing field determined from the Thellier–Thellier double heating experiment [58,59]. For this comparison, we used only those studies that reported both the intensity of NRM during stepwise demagnetization and absolute paleointensity values for H_A.

The synthetic Mars basalts have a higher χ_{TRM} than terrestrial samples (Fig. 11). Even TRM imparted at 10 μT has higher χ_{TRM} than the sample set of Carlut and Kent [56]. These results support the "magnetic telechemistry hypothesis," which proposes that iron-rich lavas generate higher concentrations of titanomagnetite and therefore record a higher-amplitude NRM [60–62].

Oxygen fugacities included in the synthesis experiments are relevant to magmatic and postmagmatic processes on Mars, as inferred from Fe–Ti oxide oxybarometry [63,64] pyroxene–melt partitioning of Eu, Gd, and Sm [30,65], olivine–spinel–pyroxene oxybarometry [31,66], and Raman spectroscopy [67] of the SNC meteorites. A consensus is emerging that the mantle source regions of the basalts represented by the SNC meteorites are less reduced than the lunar mantle, but more reduced than the terrestrial mantle [66–69]. The most reducing Martian basalt source environments are recorded in the phenocryst core compositions of Dhofar 019 (IW−0.2), and SaU 005 (IW+0.2 [66]). Other meteorites preserve evidence of near-liquidus crystallization at less reducing conditions, for example EETA 79001 lithology A (IW+2 [63]). Still other meteorites unequivocally reflect relatively oxidizing conditions in the late stages of solidification. For example, Fe–Ti oxides in Los Angeles represent conditions near QFM [70], as do the mesostases of Shergotty and MIL-03346, which contain silica, fayalite, and magnetite-rich spinel [71,72]. With the highest Fe^{3+} content recognized among the meteorites, MIL-03346 may record the most oxidizing magmatic environment yet determined for Mars [73]. Truly oxidizing conditions (MNO to MH) are not recognized in the primary igneous mineralogies of any extant meteorites, although the presence of non-terrestrial hematite in EETA-79001 [67] points to the highly oxidizing nature of the subsolidus alteration conditions this meteorite experienced. Nonetheless, Herd [66] notes that extreme fractional crystallization in a magma ocean cumulate pile may increase ferric iron to 6 wt.% and boost redox conditions close to the MH buffer. Thus, the final stages of Martian magma ocean solidification could have produced the oxidized "crust-like" component that has been proposed on the basis of oxygen isotopes and long-lived ^{147}Sm–^{143}Nd isotopic compositions of some meteorites [74]. Herd [66] suggests that interaction between reduced mantle and these late-stage "crust-like" mantle reservoirs during partial melting could give rise to the variation in intrinsic oxygen fugacities (~IW to QFM) recorded in the primary igneous minerals of the SNC meteorite suite.

Our results suggest that magmas that crystallize at or near IW conditions have a very low concentration of ferrimagnetic minerals and acquire very weak TRMs. The intensity of TRM acquired by our IW sample set is a factor of 50–500 too low to generate the observed 1000-nT anomalies within a <30-km prism. Even if the geothermal gradient allowed a prism up to 100-km thick, the IW sample set would still be a factor of 15–150 too weak to explain the MAG/ER data.

The QFM samples contain SSD to fine PSD titanomagnetite, which are very efficient carriers of TRM. The QFM samples acquired intense TRMs in weak applied fields. Although the Curie temperatures of the QFM sample set were low, 280–315 °C, the intensity of remanence, 40–200 A/m, is more than sufficient to generate 1000-nT field anomalies even in a prism as thin as 14 km (Fig. 9B).

5. Conclusions

Fe-rich basalts synthesized at variable fO_2 buffering conditions and cooling rates display a wide array of titanomagnetite crystal sizes and crystal forms. The concentration of magnetic grains, magnetic domain state, and magnetic mineralogy in the samples is highly dependent on fO_2. Within each fO_2 group there is a secondary dependence on cooling rate. Samples synthesized at IW conditions are glassy and appear paramagnetic during in-field experiments. Remanence experiments indicate the presence of a fine-grained remanence-carrier, likely near the SP/SSD boundary. While these samples acquired a measurable ARM and TRM, the intensity of TRM is a factor of 50–500 too low to account for the 1000-nT Mars crustal anomalies.

Samples synthesized at NNO and MNO conditions have a higher concentration of magnetic particles and

display large euhedral grains up to 100 μm in diameter, which is well within the multidomain range of titanomagnetite. The Fe–Ti oxide composition is Mg- and Al-bearing titanomagnetite with 2.4–2.7 Fe cations per formula unit. The Curie temperatures of these samples are up to 200 °C higher than expected for this Fe/(Ti+Mg+ Al) ratio. The elevated Curie temperatures are attributed to high-temperature deviations from stoichiometry. While the NNO and MNO samples acquired intense TRMs of 10–200 A/m, it is unlikely that any Mars magma reservoir crystallizes at such oxidizing conditions.

The QFM sample set acquired the highest intensity TRMs, up to 40 A/m in a 10-μT field and up to 200 A/m in a 50-μT field. These samples have low Curie temperatures of 285–385 °C. The depth to the QFM and MNO Curie isotherms is estimated at 14–23 km on Mars using a geothermal gradient of 25 K/km. If the geothermal gradient on Mars was 25 K/km at 4 Ga, even pure magnetite and pure hematite would have Curie isotherms shallower than ~28 km, necessitating M_Z intensities of >20 A/m to account for the total field anomalies detected by the Mars Global Surveyor MAG/ER experiment. However, the intensity of TRM acquired by our QFM sample set in a weak 10-μT field is sufficient to generate 1000-nT field anomalies at an altitude of 100 km, even in a layer as thin as 14 km. Our results suggest that Fe-rich melts that crystallize under QFM conditions will generate Timt-rich basalts that can acquire very high intensity TRMs, even in weak magnetizing fields, as postulated for the Martian magnetic field at 4 Ga.

Acknowledgements

We thank J. Marvin, M. Jackson, and P. Sølheid for their assistance during Brachfeld's visit to the IRM. We thank Jeff Gee for generously providing NRM data, and David Dunlop and an anonymous reviewer for their thoughtful, constructive comments. The Ocean Drilling Program data in Fig. 10 was generated by G. Acton, M. Antretter, C. Carvallo, R. Cottrell, M. Garces, J. Gee, H. Inokuchi, E. Kikawa, J. Tarduno, M. Torii, D. Wilson, H. Worm, and X. Zhao. This work was supported by NASA award NAG512486 from the Mars Data Analysis Program to Hammer, NASA award NNG05GL92G from the Mars Fundamental Research Program to Hammer and Brachfeld, and an IRM Visiting Fellowship. The IRM is supported by grants from the Earth Sciences Instrumentation and Facilities division of the National Science Foundation and the W. M. Keck Foundation.

References

[1] M.H. Acuña, J.E.P. Connerney, P. Wasilewski, R.P. Lin, K.A. Anderson, C.W. Carlson, J. McFadden, D.W. Curtis, D. Mitchell, H. Reme, C. Mazelle, J.A. Sauvaud, C. d'Uston, A. Cros, J.L. Medale, S.J. Bauer, P. Cloutier, M. Mayhew, D. Winterhalter, N.F. Ness, Magnetic field and plasma observations at Mars: initial results of the Mars Global Surveyor Mission, Science 279 (1998) 1676–1680.

[2] M.H. Acuña, J.E.P. Connerney, N.F. Ness, R.P. Lin, D. Mitchell, C.W. Carlson, J. McFadden, K.A. Anderson, H. Rème, C. Mazelle, D. Vignes, P. Wasilewski, P. Cloutier, Global distribution of crustal magnetization discovered by the Mars Global Surveyor MAG/ER Experiment, Science 284 (1999) 790–793.

[3] J.E.P. Connerney, M.H. Acuña, P.J. Wasilewski, N.F. Ness, H. Rème, C. Mazelle, D. Vignes, R.P. Lin, D.L. Mitchell, P.A. Cloutier, Magnetic lineations in the ancient crust of Mars, Science 284 (1999) 794–798.

[4] J.E.P. Connerney, M.H. Acuña, P.J. Wasilewski, G. Kletetschka, N.F. Ness, H. Rème, R.P. Linn, D.L. Mitchell, The global magnetic field of Mars and implications for crustal evolution, Geophys. Res. Lett. 28 (21) (2001) 4015–4018.

[5] M. Purucker, D. Ravat, H. Frey, C. Voorhies, T. Sabaka, M. Acuña, An altitude-normalized magnetic map of Mars and its interpretation, Geophys. Res. Lett. 27 (2000) 2449–2452.

[6] A.G. Fairen, J. Ruiz, F. Anguita, An origin for the linear magnetic anomalies on Mars through accretion of terranes: implications for dynamo timing, Icarus 160 (2002) 220–223.

[7] F. Nimmo, Dike intrusion as a possible cause of linear Martian magnetic anomalies, Geology 28 (2000) 391–394.

[8] E.D. Scott, M. Fuller, A possible source for the Martian crustal magnetic field, Earth Planet. Sci. Lett. 220 (2004) 83–90.

[9] J.L. Bandfield, V.E. Hamilton, P.R. Christensen, A global view of Martian surface compositions from MGS–TES, Science 287 (2000) 1626–1630.

[10] S.M. Cisowski, M. Fuller, The effect of shock on the magnetism of terrestrial rocks, J. Geophys. Res. 83 (B7) (1978) 3441–3458.

[11] P. Rochette, G. Fillion, R. Ballou, F. Brunet, B. Ouladdiaf, L. Hood, High pressure magnetic transition in pyrrhotite and impact demagnetization on Mars, Geophys. Res. Lett. 30 (13) (2003) 1683.

[12] L.L. Hood, N.C. Richmond, E. Pierazzo, P. Rochette, Distribution of crustal magnetic fields on Mars: shock effects of basin-forming impacts, Geophys. Res. Lett. 30 (6) (2003) 1281, doi:10.1029/2002GL016657.

[13] P.S. Mohit, J. Arkani-Hamed, Impact demagnetization of the Martian crust, Icarus 168 (2004) 305–317.

[14] G. Kletetschka, J.E.P. Connerney, N.F. Ness, M.H. Acuña, Pressure effects on Martian crustal magnetization near large impact basins, Meteorit. Planet. Sci. 39 (2004) 1–10.

[15] T.N. Nagata, Paleomagnetism of Antarctic achondrites, Mem. Natl. Inst. Polar Res., Spec. Issue 17 (1980) 233–242.

[16] S.M. Cisowski, Magnetic studies on Shergotty and other SNC meteorites, Geochim. Cosmochim. Acta 50 (1986) 1043–1048.

[17] D.W. Collinson, Magnetic properties of Antarctic shergottite meteorites EETA 79001 and ALHA 77005: possible relevance to a Martian magnetic field, Earth Planet. Sci. Lett. 77 (1986) 159–164.

[18] D.W. Collinson, Magnetic properties of Martian meteorites: implications for an ancient Martian magnetic field, Meteorit. Planet. Sci. 32 (1997) 803–811.

[19] J. Shaw, M.J. Hill, S.J. Openshaw, Investigating the ancient Martian magnetic field using microwaves, Earth Planet. Sci. Lett. 190 (2001) 103–109.

[20] P. Rochette, J.P. Lorand, G. Fillion, V. Sautter, Pyrrhotite and the remanent magnetization of SNC meteorites: a changing perspective on Martian magnetism, Earth Planet. Sci. Lett. 190 (2001) 1–12.
[21] B.P. Weiss, H. Vali, F.J. Baudenbacher, J.L. Kirschvink, S.T. Stewart, D.L. Shuster, Records of an ancient Martian magnetic field in ALH84001, Earth Planet. Sci. Lett. 201 (2002) 449–463.
[22] M. Antretter, M. Fuller, E. Scott, M. Jackson, B. Moskowitz, P. Sølheid, Paleomagneitc record of Martian meteorite ALH84001, J. Geophys. Res. 108 (E6) (2003) 5049, doi:10.1029/2002JE001979.
[23] Y. Yu, J.S. Gee, Spinel in Martian meteorite SaU 008: implications for Martian magnetism, Earth Planet. Sci. Lett. 232 (2005) 287–294.
[24] G. Kletetschka, P.J. Wasilewski, P.T. Taylor, Hematite vs. magnetite as the signature for planetary magnetic anomalies? Phys. Earth Planet. Int. 119 (2000) 259–267.
[25] G. Kletetschka, P.J. Wasilewski, P.T. Taylor, Unique thermoremanent magnetization of multidomain sized hematite: implications for magnetic anomalies, Earth Planet. Sci. Lett. 176 (2000) 469–479.
[26] G. Kletetschka, P.J. Wasilewski, P.T. Taylor, Mineralogy of the sources for magnetic anomalies on Mars, Meteorit. Planet. Sci. 35 (2000) 895–899.
[27] D.J. Dunlop, G. Kletetschka, Multidomain hematite: a source of planetary magnetic anomalies? Geophys. Res. Lett. 28 (2001) 3345–3348.
[28] G. Kletetschka, M.H. Acuña, T. Kohout, P.J. Wasilewski, J.E.P. Connerney, An empirical scaling law for acquisition of thermoremanent magnetization, Earth Planet. Sci. Lett. 226 (2004) 521–528.
[29] G. Kletetschka, N.F. Ness, J.E.P. Connerney, M.H. Acuña, P.J. Wasilewski, Grain size dependent potential for self generation of magnetic anomalies on Mars via thermoremanent magnetic acquisition and magnetic interaction of hematite and magnetite, Phys. Earth Planet. Int. 148 (2005) 149–156.
[30] M. Wadhwa, Redox state of Mars' upper mantle and crust from Eu anomalies in shergottite pyroxenes, Science 291 (2001) 1527–1530.
[31] C.D.K. Herd, L.E. Borg, J.H. Jones, J.J. Papike, Oxygen fugacity and geochemical variations in the Martian basalts: implications for Martian basalt petrogenesis and the oxidation state of the upper mantle of Mars, Geochim. Cosmochim. Acta 66 (2002) 2025–2036.
[32] L.E. Nyquist, D.D. Bogard, C.Y. Shih, A. Greshake, D. Stoffler, O. Eugster, Ages and geologic histories of Martian meteorites, Space Sci. Rev. 96 (2001) 105–164.
[33] J.E. Hammer, S. Brachfeld, M.J. Rutherford, LPSC XXXIV, LPI, Houston, TX, 2003.
[34] J. Hammer, Dynamic crystallization of Fe-rich basalt: fO_2 and cooling rate controls on the kinetics and energetics of solidification, Earth Planet. Sci. Lett. 248 (2006) 618–637 (this volume). doi:10.1016/j.epsl.2006.04.022.
[35] D.H. Lindsley, The crystal chemistry and structure of oxide minerals as exemplified by the Fe–Ti oxides, Rev. Min. 3 (1976) L1–L60.
[36] D.J. Dunlop, Ö. Özdemir, Rock Magnetism: Fundamentals and Frontiers, Cambridge University Press, Cambridge, 1997.
[37] G.R. Olhoeft, G.R. Johnson, Densities of rocks and minerals, in: R.S. Carmichael (Ed.), CRC Practical Handbook of Physical Properties of Rocks and Minerals, CRC Press, Inc., 1989.
[38] R. Butler, Paleomagnetism, Paleomagnetism: Magnetic Domains to Geologic Terranes, Blackwell Scientific, 1992.
[39] R. Day, M.D. Fuller, V.A. Schmidt, Hysteresis properties of titanomagnetites: grain size and composition dependence, Phys. Earth Planet. Int. 13 (1977) 260–266.
[40] H.-U. Worm, On the superparamagnetic-stable single domain transition for magnetite, and frequency dependence of susceptibility, Geophys. J. Int. 133 (1998) 201–206.
[41] B.M. Moskowitz, M. Jackson, C. Kissel, Low-temperature magnetic behavior of titanomagnetites, Earth Planet. Sci. Lett. 157 (1998) 141–149.
[42] Ö. Özdemir, D. Dunlop, Low-temperature behavior and memory of iron-rich titanomagnetites (Mt. Haruna, Japan and Mt. Pinatubo, Philippines), Earth Planet. Sci. Lett. 216 (2003) 193–200.
[43] Z. Hauptman, High temperature oxidation, range of non-stoichiometry and Curie point variation of cation-deficient titanomagnetite $Fe_{2.4}Ti_{0.6}O_{4+\gamma}$, Geophys. J. R. Astron. Soc. 38 (1974) 29–47.
[44] B.J. Wanamaker, B.M. Moskowitz, Effect of nonstoichiometry on the magnetic and electrical properties of synthetic single crystal $Fe_{2.4}Ti_{0.6}O_4$, Geophys. Res. Lett. 21 (1994) 983–986.
[45] P.W. Readman, W. O'Reilly, Magnetic properties of oxidized (cation-deficient) titanomagnetites (Fe, Ti, [])$_3O_4$, J. Geomagn. Geoelectr. 24 (1972) 69–90.
[46] Ö. Özdemir, S.K. Banerjee, High temperature stability of maghemite γFe_2O_3, Geophys. Res. Lett. 11 (1984) 161–164.
[47] F. Nimmo, M.S. Gilmore, Constraints on the depth of magnetized crust on Mars from impact craters, J. Geophys. Res. 106 (2001) 12315–12323.
[48] F. Nimmo, D. Stevenson, Estimates of Martian crustal thickness from viscous relaxation of topography, J. Geophys. Res. 106 (2001) 5085–5098.
[49] B.L. Isacks, Calculation of sea floor spreading anomalies, Cornell University, 1–23, 1996 (unpublished report, Available online).
[50] H.J.B. Dick, J.H. Natland, D.J. Miller, et al., Proc. ODP, Initial Rep. 176 (1999) [Online]. Available from World Wide Web: <http://www-odp.tamu.edu/publications/176_IR/176TOC.HTM>. [Cited 2005-09-03].
[51] M.F. Coffin, F.A. Frey, P.J. Wallace, et al., Proc. ODP, Initial Rep. 183 (2000) [Online]. Available from World Wide Web:<http://www-odp.tamu.edu/publications/183_IR/183ir.htm>. [Cited 2005-09-03].
[52] J.A. Tarduno, R.A. Duncan, D.W. Scholl, et al., Proc. ODP, Initial Rep. 197 (2002) [Online]. Available from World Wide Web: http://www-odp.tamu.edu/publications/197_IR/197ir.htm. [Cited 2005-09-03].
[53] D.S. Wilson, D.A.H. Teagle, G.D. Acton, et al., Proc. ODP, Initial Rep. 206 (2003) [Online]. Available from World Wide Web: http://www-odp.tamu.edu/publications/206_IR/206ir.htm. [Cited 2005-09-03].
[54] P.B. Kelemen, E. Kikawa, D.J. Miller, et al., Proc. ODP, Initial Rep. 209 (2004) [Online]. Available from World Wide Web: http://www-odp.tamu.edu/publications/209_IR/209ir.htm. [Cited 2005-09-03].
[55] A. Raïs, C. Laj, J. Surmont, P.-Y. Gillot, H. Guillou, Geomagnetic field intensity between 70 000 and 130 000 years B.P. from a volcanic sequence on la Réunion, Indian Ocean, Earth Planet. Sci. Lett. 140 (1996) 173–189.
[56] J. Carlut, D.V. Kent, Grain-size-dependent paleointensity results from very recent mid-oceanic ridge basalts, J. Geophys. Res. 107 (B3) (2002)10.1029/2001JB000439.
[57] M.T. Juárez, L. Tauxe, J.S. Gee, T. Pick, The intensity of the Earth's magnetic field over the past 160 million years, Nature 394 (1998) 878–881.
[58] E. Thellier, O. Thellier, Sur l'intensite´ du champ magnétique terrestre dans le passé historique et géologique, Ann. Geophys. 15 (1959) 285–376.

[59] R.S. Coe, Paleointensities of the Earth's magnetic field determined from Tertiary and Quaternary rocks, J. Geophys. Res. 72 (1967) 3247–3262.
[60] P.R. Vogt, G.L. Johnson, Magnetic telechemistry of oceanic crust? Nature 245 (1973) 373–375.
[61] P.R. Vogt, Amplitudes of oceanic magnetic anomalies and the chemistry of oceanic crust: synthesis and review of 'magnetic telechemistry', Can. J. Earth Sci. 16 (1979) 2236–2262.
[62] J. Gee, D.V. Kent, Magnetization of axial lavas from the southern East Pacific Rise (14–23°S): geochemical controls on magnetic properties, J. Geophys. Res. 102 (B11) (1997) 24873–24886.
[63] S. Ghosal, R.O. Sack, M.S. Ghiorso, M.E. Lipschutz, Evidence for a reduced, Fe-depleted Martian mantle source region of shergottites, Contrib. Mineral. Petrol. 130 (1998) 346–357.
[64] C.D.K. Herd, J.J. Papike, A.J. Brearley, Oxygen fugacity of Martian basalts from electron microprobe oxygen and TEM–EELS analyses of Fe–Ti oxides, Am. Mineral. 86 (2001) 1015–1024.
[65] M.C. McCanta, M.J. Rutherford, J.H. Jones, An experimental study of rare earth element partitioning between a shergottite melt and pigeonite: implications for the oxygen fugacity of the Martian interior, Geochim. Cosmochim. Acta 68 (2004) 1943–1952.
[66] C.D.K. Herd, The oxygen fugacity of olivine–phyric Martian basalts and the components within the mantle and crust of Mars, Meteorit. Planet. Sci. 38 (2003) 1793–1805.
[67] A. Wang, K.E. Kuebler, B.L. Jolliff, L.A. Haskin, Raman spectroscopy of Fe–Ti–Cr–oxides, case study: Martian meteorite EETA79001, Am. Mineral. 89 (2004) 665–680.
[68] J.J. Papike, J.M. Karner, C.K. Shearer, Comparative planetary mineralogy: valence state partitioning of Cr, Fe, Ti, and V among crystallographic sites in olivine, pyroxene, and spinel from planetary basalts, Am. Mineral. 90 (2005) 277–290.
[69] D. Canil, Vanadium partitioning between orthopyroxene, spinel and silicate melt and the redox states of mantle source regions for primary magmas, Geochim. Cosmochim. Acta 63 (1999) 557–572.
[70] A.E. Rubin, P.H. Warren, J.P. Greenwood, R.S. Verish, L.A. Leshin, R.L. Hervig, R.N. Clayton, T.K. Mayeda, Los Angeles: the most differentiated basaltic Martian meteorite, Geology 28 (2000) 1011–1014.
[71] J.E. Hammer, M.J. Rutherford, Experimental crystallization of Fe-rich basalt: application to cooling rate and oxygen fugacity of Nakhlite MIL-03346 (abstract #1999), in: 36th Lunar and Planetary Science Conference CD-ROM, 2005.
[72] V.P.S. Hale, H.Y. McSween, G.A. McKay, Re-evaluation of intercumulus liquid composition and oxidation state for the Shergotty meteorite, Geochim. Cosmochim. Acta 63 (1999) 1459–1470.
[73] M.D. Dyar, A.H. Treiman, C.M. Pieters, T. Hiroi, M.D. Lane, V. O'Connor, MIL03346, the most oxidized Martian meteorite: a first look at spectroscopy, petrography, and mineral chemistry, J. Geophys. Res. 110 (2005).
[74] L.E. Borg, D.S. Draper, A petrogenetic model for the origin and compositional variation of the Martian basaltic meteorites, Meteorit. Planet. Sci. 38 (2003) 1713–1731.